Defects of the nearest-neighbor tight-binding model in the study of solid harmonics

Yupeng Zhang ,[1,2,3] Mingying Zhang ,[1,2,3] Wenli Yang ,[1,2,3] Haiyuan Yu,[1,2,3] M. S. Si,[4] Shan Xue,[1,2,3,*]
and Hongchuan Du [1,2,3,†]

[1]*Frontiers Science Center for Rare Isotopes, Lanzhou University, Lanzhou 730000, China*
[2]*School of Nuclear Science and Technology, Lanzhou University, Lanzhou 730000, China*
[3]*Key Laboratory of Special Function Materials and Structure Design, Ministry of Education, Lanzhou University, Lanzhou 730000, China*
[4]*Key Laboratory for Magnetism and Magnetic Materials of the Ministry of Education, Lanzhou University, Lanzhou 730000, China*

At present, the nearest-neighbor tight-binding model is often used to study the high-order harmonic generation (HHG) in solids, but its defects are little known. We theoretically investigate the defects of the nearest-neighbor tight-binding model in the study of solid HHG by developing the semiconductor Bloch equations with the accelerated Bloch-like basis consisting of the maximally localized Wannier functions. To achieve this goal, we calculate the harmonic spectra, orientation and ellipticity dependence of harmonic yield in monolayer black phosphorus using the nearest-neighbor tight-binding model, and the *ab initio* model, respectively. It is found that there are obvious differences between the calculation results of the two models. This indicates the limitations of the nearest-neighbor tight-binding approximation in the study of solid HHG. Furthermore, we study the role of the matrix elements of the position operator under the Wannier basis in solid HHG, which are often discarded in many previous works. It is found that these matrix elements have an important influence on the orientation and ellipticity dependence of higher-order harmonic yield. This work remedies some defects of previous theories and will greatly promote the accurate calculation of strong-field nonlinear responses in solids.

I. INTRODUCTION

High-order harmonic generation (HHG) is an important nonlinear optical phenomenon in the interaction between intense laser and matters. In the past decades, HHG in gases has attracted wide attention for its applications in generating attosecond light pulses and coherent soft x rays [1–5], extracting the ionization times [6–8], probing ultrafast dynamics of atoms and molecules [9–11], imaging molecular orbitals [12], and so on. Due to the low conversion efficiency of HHG in gases, attention has been turned to HHG in solids. Many interesting phenomena are found in solid HHG, such as the linear relationship between the cutoff energy and laser electric field amplitude [13], anomalous ellipticity dependence [14–19], multiplateau structures [20–24], and complex orientation dependence [14,25–30]. In addition, solid HHG has promising applications in developing compact coherent extreme ultraviolet light sources [31,32], reconstructing band structure [33–37], probing Berry curvature [38], researching topological phase transitions [39–43], imaging valence electrons with picometre resolution [44], and so on.

Despite much progress in the study of solid HHG, theoretical calculations still face challenges in reproducing experimental results. For example, even-order harmonics are observed at certain orientation angles in the experiments of ZnO [13,26], which could not be reproduced in earlier

theoretical investigations [45,46]. Recently, Jiang *et al.* successfully reproduced the orientation dependence of harmonic yield in ZnO by considering the phases of the transition dipole matrix elements [47,48]. In addition, the Berry connections are generally nonzero in systems without spatial inversion symmetry, and were also neglected in earlier works. In our recent work, we revealed the importance of Berry connections in solid HHG, and proved that the semiconductor Bloch equations (SBEs) are gauge invariant only when Berry connections are contained [49]. However, in numerical calculations, the Bloch functions are often obtained by the diagonalization performed separately for each crystal momentum, so they usually carry random phases and are discontinuous and noperiodic. This makes it difficult to calculate the derivative term and interpolation of the transition dipole matrix elements and Berry connections. One way to cure this problem is to construct smooth Bloch-like functions directly using the maximally localized Wannier functions (MLWF) [50,51]. Recently, Sliva *et al.* developed the SBEs in the length gauge with the Wannier basis [52]. However, the number of sampling points in the first Brillouin zone (BZ) must be dense enough for convergence due to the gradient term in the equations, which greatly limits the calculation efficiency and makes it difficult to apply this method to systems with higher dimensions and more energy bands. In previous work, we found that, by adopting the adiabatic Houston basis, the gradient term can be replaced by the time-dependent crystal momentum $\boldsymbol{k}(t) = \boldsymbol{k}_0 + \boldsymbol{A}(t)$ so that the calculation efficiency can be significantly improved [53]. Therefore, it is one of our aims to develop the SBEs with the accelerated Bloch-like basis consisting of the MLWF.

*xues@lzu.edu.cn
†duhch@lzu.edu.cn

Nowadays, the semiempirical nearest-neighbor tight-binding (NNTB) model is widely used in solid HHG calculations [54–57]. However, the electronic structure information obtained by the NNTB model may be inaccurate because of the two primary approximations. One is the NNTB approximation, and the other one is that the matrix elements of the position operator $\hat{r}$ in the Wannier basis are often neglected [58,59]. It was found that these matrix elements cannot be discarded when calculating the dielectric function and shift photoconductivity [60]. However, how these approximations affect the calculation of solid harmonics is still an open question so far.

Two-dimensional (2D) materials with ultrathin atomic layer thicknesses have excellent electronic, optical, sensing, and electrochemical properties, and provide new research directions in the fields of nanoelectronic devices, materials science, condensed matter physics, biomedicine, and so on [61–64]. HHG in 2D materials has also attracted great attention in recent years [16,25,65,66]. As a typical 2D material, monolayer black phosphorus (BP) has many distinctive properties, such as direct and tunable band gap, high carrier mobility, and in-plane anisotropy [67–69]. HHG in monolayer BP also shows higher intensity and cutoff energy than graphene, MoS_2, and hexagonal boron nitride [70]. However, there is still a lack of the orientation and ellipticity dependence of harmonic yield in monolayer BP. Therefore, this work has three purposes. First, we develop the SBEs with the accelerated Bloch-like basis consisting of the MLWF. Second, we investigate the orientation and ellipticity dependence of harmonic yield in monolayer BP. Finally, we explore the limitations of the NNTB model by means of HHG in monolayer BP.

This paper is organized as follows. In Sec. II, we derive the SBEs with the accelerated Bloch-like basis consisting of the MLWF and construct the NNTB model of monolayer BP. In Sec. III, the orientation and ellipticity dependence of harmonic yield in monolayer BP are investigated in detail. In Sec. III A, we demonstrate the validity of our developed SBEs, and study the limitations of the NNTB approximation. In Sec. III B, we focus on the role of the matrix elements of the position operator in solid HHG. In Sec. III C, we discuss the effect of defferent dephasing times on the harmonic spectra. Finally, a summary is given in Sec. IV. Atomic units are used throughout unless otherwise stated.

II. THEORETICAL METHOD

A. Advantage of the Wannier gauge

For crystals that contain N_c unitary cells, the Bravais lattice vectors are $\boldsymbol{R} = \sum_i n_i \boldsymbol{a}_i (i = 1, 2, 3)$, where $\boldsymbol{a}_i$ are the primitive vectors. A set of localized Wannier functions can be expressed as $w_m(\boldsymbol{r} - \boldsymbol{R}) = \langle \boldsymbol{r}|\boldsymbol{R}m\rangle$, where m runs over all the Wannier orbitals. The set of Wannier functions forms an orthonormal basis, namely, $\langle \boldsymbol{0}m|\boldsymbol{R}n\rangle = \delta_{\boldsymbol{0R}}\delta_{mn}$. Then the Bloch-like functions can be given by

$$\left|\phi_{m\boldsymbol{k}}^{(W)}\right\rangle = \frac{1}{\sqrt{N_c}} \sum_{\boldsymbol{R}} e^{i\boldsymbol{k}\cdot\boldsymbol{R}}|\boldsymbol{R}m\rangle, \quad (1)$$

where m is the band index and $\boldsymbol{k}$ is the wave vector in reciprocal space. The Bloch-like functions are also orthogonal, namely, $\langle \phi_{m\boldsymbol{k}}^{(W)}|\phi_{n\boldsymbol{k}'}^{(W)}\rangle = \delta_{mn}\delta_{\boldsymbol{kk}'}$. Accordingly, in the Wannier gauge, the matrix elements of Hamiltonian and transition dipole moment can be defined as [52,71]

$$H_{mn,\boldsymbol{k}}^{(W)} = \left\langle \phi_{m\boldsymbol{k}}^{(W)}\big|\hat{H}_0\big|\phi_{n\boldsymbol{k}}^{(W)}\right\rangle \equiv \sum_{\boldsymbol{R}} e^{i\boldsymbol{k}\cdot\boldsymbol{R}}\langle \boldsymbol{0}m|\hat{H}_0|\boldsymbol{R}n\rangle, \quad (2)$$

$$\boldsymbol{A}_{mn,\boldsymbol{k}}^{(W)} = \left\langle u_{m\boldsymbol{k}}^{(W)}\big|i\nabla_{\boldsymbol{k}}\big|u_{n\boldsymbol{k}}^{(W)}\right\rangle \equiv \sum_{\boldsymbol{R}} e^{i\boldsymbol{k}\cdot\boldsymbol{R}}\langle \boldsymbol{0}m|\hat{\boldsymbol{r}}|\boldsymbol{R}n\rangle, \quad (3)$$

where the sum of $\boldsymbol{R}$ runs over all lattice vectors, $|u_{n\boldsymbol{k}}^{(W)}\rangle$ is the periodic part of the Bloch-like functions, $\hat{H}_0$ and $\hat{\boldsymbol{r}}$ are the unperturbed Hamiltonian and position operator, respectively. The superscript (W) refers to the Wannier gauge. These two matrices are smooth with $\mathbf{k}$ and can be transformed to the Hamiltonian gauge (H) by diagonalizing $H^{(W)}(\boldsymbol{k})$, which allows them to effectively operate within the Bloch basis. We can diagonalize the Hamiltonian matrix $H^{(W)}(\boldsymbol{k})$ with a unitary matrix: [52,71]

$$H^{(H)}(\boldsymbol{k}) = U^{\dagger}(\boldsymbol{k})H^{(W)}(\boldsymbol{k})U(\boldsymbol{k}), \quad (4)$$

and the corresponding matrix $A^{(H)}(\boldsymbol{k})$ can be given by

$$\boldsymbol{A}^{(H)}(\boldsymbol{k}) = U^{\dagger}(\boldsymbol{k})\boldsymbol{A}^{(W)}(\boldsymbol{k})U(\boldsymbol{k}) + iU^{\dagger}(\boldsymbol{k})\frac{\partial}{\partial\boldsymbol{k}}U(\boldsymbol{k}), \quad (5)$$

where $H^{(H)}$ and $\boldsymbol{A}^{(H)}$ are the Hamiltonian matrix and transition dipole matrix under the Bloch basis, respectively, and $U(\boldsymbol{k})$ is the unitary matrix that diagonalizes $H^{(W)}$.

The diagonalized Hamiltonian describes the eigenenergy of the system, i.e., $H_{mn}^{(H)}(\boldsymbol{k}) = \epsilon_n(\boldsymbol{k})\delta_{mn}$. The corresponding Bloch states are

$$\left|\phi_{m\boldsymbol{k}}^{(H)}\right\rangle = \sum_n U_{nm}(\boldsymbol{k})\left|\phi_{n\boldsymbol{k}}^{(W)}\right\rangle. \quad (6)$$

These transformations of Eqs. (4) and (5) are transformations between operator matrices at different basis, and Eq. (6) is a unitary transformation of a different basis. In general, the matrix $U(\boldsymbol{k})$ is not unique and contains random phases. This makes it difficult to ensure that $A^{(H)}(\boldsymbol{k})$ is smooth with respect to $\boldsymbol{k}$. Therefore, we choose to solve the SBEs in the Wannier gauge.

B. SBEs in the Wannier gauge

To describe the interaction between intense laser and solids, we start with the single-particle time-dependent Schrödinger equation (TDSE) with the dipole approximation and the velocity gauge, the time evolution of an electron under laser field can be described as

$$i\frac{\partial}{\partial t}\psi(\boldsymbol{r}, t) = \hat{H}(t)\psi(\boldsymbol{r}, t), \quad (7)$$

$$\hat{H}(t) = \frac{1}{2}[\hat{p} + \mathbf{A}(t)]^2 + V(\boldsymbol{r}), \quad (8)$$

where $\mathbf{A}(t)$ is the vector potential of laser field, $V(\boldsymbol{r})$ is the periodic potential of crystals. By using the acceleration theorem of Bloch electrons [72–74], we construct an adiabatic instantaneous eigenstate of Eq. (7), the Houston state $\widetilde{\phi}_{n\boldsymbol{k}}(\boldsymbol{r}, t) = e^{-i\mathbf{A}(t)\cdot\boldsymbol{r}}\phi_{n\boldsymbol{k}}(\boldsymbol{r})$, which satisfies

$$\hat{H}(t)\widetilde{\phi}_{n\boldsymbol{k}}(\boldsymbol{r}, t) = \varepsilon_n^{\boldsymbol{k}}\widetilde{\phi}_{n\boldsymbol{k}}(\boldsymbol{r}, t). \quad (9)$$

Then the electronic wave function can be expanded as

$$
\begin{aligned}
\psi(\boldsymbol{r}, t) &= \int_{BZ} \sum_n C_n^{\boldsymbol{k}}(t) \widetilde{\phi}_{n\boldsymbol{k}}(\boldsymbol{r}, t) d\boldsymbol{k} \\
&= \int_{BZ} \sum_n C_n^{\boldsymbol{k}}(t) e^{-i\mathbf{A}(t)\cdot\boldsymbol{r}} \phi_{n\boldsymbol{k}}(\boldsymbol{r}) d\boldsymbol{k},
\end{aligned} \tag{10}
$$

where $\phi_{n\boldsymbol{k}}(\boldsymbol{r}) = \langle \boldsymbol{r}|\phi_{n\boldsymbol{k}}\rangle$. The corresponding density matrix elements can be given by

$$
\rho_{nm}^{\boldsymbol{k}}(t) = C_m^{*\boldsymbol{k}}(t) C_n^{\boldsymbol{k}}(t). \tag{11}
$$

By substituting Eqs. (9), (10), and (11) into Eq. (7), we can get the SBEs in the Wannier gauge

$$
\begin{aligned}
&\frac{\partial \rho_{nm}^{(W)\boldsymbol{k}_0}(t)}{\partial t} \\
&= i \sum_l \left[H_{lm}^{(W)\boldsymbol{k}(t)} \rho_{nl}^{(W)\boldsymbol{k}_0}(t) - H_{nl}^{(W)\boldsymbol{k}(t)} \rho_{lm}^{(W)\boldsymbol{k}_0}(t) \right] \\
&\quad + i\boldsymbol{E}(t) \cdot \sum_l \left[\boldsymbol{A}_{lm}^{(W)\boldsymbol{k}(t)} \rho_{nl}^{(W)\boldsymbol{k}_0}(t) - \boldsymbol{A}_{nl}^{(W)\boldsymbol{k}(t)} \rho_{lm}^{(W)\boldsymbol{k}_0}(t) \right].
\end{aligned} \tag{12}
$$

Here, $\boldsymbol{E}(t)$ is the laser electric field. The crystal momentum $\boldsymbol{k}(t) = \boldsymbol{k}_0 + \mathbf{A}(t)$ is time-dependent, where $\boldsymbol{k}_0$ is the initial crystal momentum of electron before the laser pulse arrives.

In the SBEs, the dephasing term is often used to describe the decoherence caused by the electron-electron and electron-phonon scattering, which makes the calculation results to be more consistent with experiments [54]. In the calculations, the dephasing term can be handled in the Hamiltonian gauge. In other words, we can propagate the coherent equations in the Wannier gauge and consider the decoherent part in the Hamiltonian gauge [52]. The equations in the Hamiltonian gauge read

$$
\begin{aligned}
&\frac{\partial \rho_{nm}^{(H)\boldsymbol{k}_0}(t)}{\partial t} \\
&= i \sum_l \left[H_{lm}^{(H)\boldsymbol{k}(t)} \rho_{nl}^{(H)\boldsymbol{k}_0}(t) - H_{nl}^{(H)\boldsymbol{k}(t)} \rho_{lm}^{(H)\boldsymbol{k}_0}(t) \right] \\
&\quad + i\boldsymbol{E}(t) \cdot \sum_l \left[\boldsymbol{A}_{lm}^{(H)\boldsymbol{k}(t)} \rho_{nl}^{(H)\boldsymbol{k}_0}(t) - \boldsymbol{A}_{nl}^{(H)\boldsymbol{k}(t)} \rho_{lm}^{(H)\boldsymbol{k}_0}(t) \right] \\
&\quad - \frac{(1 - \delta_{nm})}{T_2} \rho_{nm}^{(H)\boldsymbol{k}_0}(t),
\end{aligned} \tag{13}
$$

where T_2 is the dephasing time.

In the Hamiltonian gauge, the initial condition of the system is assumed to be that the electrons are full occupied in the valence bands and has no coherences between eigenstates, i.e., $\rho_{nn}^{(H)}(\boldsymbol{k}) = 1$ (n runs over all valence bands) and $\rho_{nm}^{(H)}(\boldsymbol{k}) = 0$ ($n \neq m$). In the Wannier gauge, the initial density matrix elements can be obtained by the following transformation:

$$
\rho^{(W)}(\boldsymbol{k}, t) = U(\boldsymbol{k}) \rho^{(H)}(\boldsymbol{k}, t) U^\dagger(\boldsymbol{k}). \tag{14}
$$

After obtaining the time-dependent density matrix, the electric current can be given by

$$
\begin{aligned}
\boldsymbol{J}(t) = -\sum_{m,n} \int_{BZ} & \left[\rho_{nm}^{(W)\boldsymbol{k}_0}(t) \boldsymbol{p}_{mn}^{(W)\boldsymbol{k}(t)} \right. \\
& \left. + \sum_l i\rho_{nm}^{(W)\boldsymbol{k}_0}(t) \left(H_{ln}^{(W)\boldsymbol{k}(t)} \boldsymbol{A}_{ml}^{(W)\boldsymbol{k}(t)} - H_{ml}^{(W)\boldsymbol{k}(t)} \boldsymbol{A}_{ln}^{(W)\boldsymbol{k}(t)} \right) \right] d\boldsymbol{k},
\end{aligned} \tag{15}
$$

with the momentum matrix elements $\boldsymbol{p}_{mn}^{\boldsymbol{k}} = \langle \widetilde{\phi}_m^{\boldsymbol{k}} | \hat{\boldsymbol{p}} | \widetilde{\phi}_n^{\boldsymbol{k}} \rangle$. Then the high-order harmonic spectra is obtained by the modulus square of current Fourier transform.

The current can be divided into the intraband and interband component in the Hamiltonian gauge [52]

$$
\begin{aligned}
\boldsymbol{J}_{\text{intra}}(t) &= -\sum_n \int_{BZ} \boldsymbol{p}_{nn}^{(H)\boldsymbol{k}(t)} \rho_{nn}^{(H)\boldsymbol{k}_0}(t) d\boldsymbol{k} \\
&= -\sum_n \int_{BZ} (\nabla_{\boldsymbol{k}} \varepsilon_n^{\boldsymbol{k}(t)}) \rho_{nn}^{(H)\boldsymbol{k}_0}(t) d\boldsymbol{k},
\end{aligned} \tag{16a}
$$

$$
\begin{aligned}
\boldsymbol{J}_{\text{inter}}(t) &= \sum_{m\neq n,l} \int_{BZ} i\rho_{mn}^{(H)\boldsymbol{k}_0}(t) \left(H_{ln}^{(H)\boldsymbol{k}(t)} \boldsymbol{A}_{ml}^{(H)\boldsymbol{k}(t)} - H_{ml}^{(H)\boldsymbol{k}(t)} \boldsymbol{A}_{ln}^{(H)\boldsymbol{k}(t)} \right) d\boldsymbol{k} \\
&= -\sum_{m\neq n} \int_{BZ} i\rho_{mn}^{(H)\boldsymbol{k}_0}(t) (\varepsilon_m^{\boldsymbol{k}(t)} - \varepsilon_n^{\boldsymbol{k}(t)}) [(U^\dagger \boldsymbol{A}^{(W)} U)_{mn}^{\boldsymbol{k}(t)} + \boldsymbol{d}_{mn}^{(H)\boldsymbol{k}(t)}] d\boldsymbol{k},
\end{aligned} \tag{16b}
$$

where $\boldsymbol{d}_{mn}^{(H)\boldsymbol{k}}$ is the transition dipole moment in the accelerated Bloch basis.

In the tight-binding model, the matrix elements of Hamiltonian are established by the on-site energies ϵ_m and hopping matrix elements

$$
\langle \mathbf{0}m|\hat{H}|\boldsymbol{R}n\rangle = \epsilon_m \delta_{\mathbf{0R}} \delta_{mn} + t_{mn}(\boldsymbol{R}), \tag{17}
$$

and the matrix elements of the position operator can be similarly given by

$$
\langle \mathbf{0}m|\hat{\boldsymbol{r}}|\boldsymbol{R}n\rangle = \boldsymbol{\tau}_m \delta_{\mathbf{0R}} \delta_{mn} + \boldsymbol{d}_{mn}(\boldsymbol{R}), \tag{18}
$$

where $\boldsymbol{\tau}_m$ is the center of the mth Wannier orbital. However, we find that the matrix elements of position operator are often neglected in previous works [58,59]. In this case, $\boldsymbol{A}_{mn,\boldsymbol{k}}^{(W)}$ in Eq. (3) is zero and Eq. (12) becomes

$$
\frac{\partial \rho_{nm}^{(W)\boldsymbol{k}_0}(t)}{\partial t} = i \sum_l \left[H_{lm}^{(W)\boldsymbol{k}(t)} \rho_{nl}^{(W)\boldsymbol{k}_0}(t) - H_{nl}^{(W)\boldsymbol{k}(t)} \rho_{lm}^{(W)\boldsymbol{k}_0}(t) \right], \tag{19}
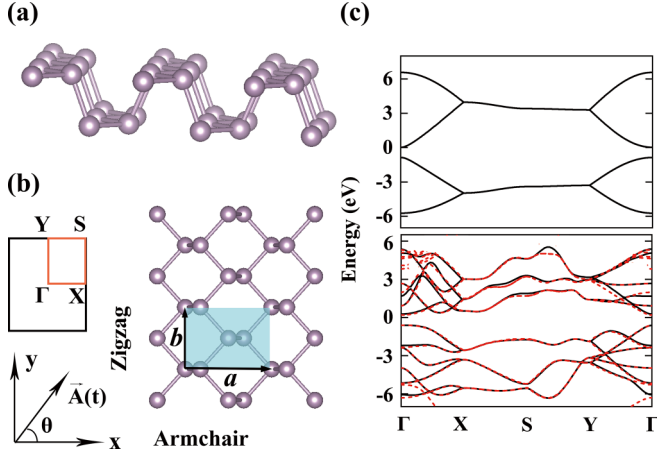$$

(a)

(b)

(c)

FIG. 1. (a) Side view of the crystal structure of monolayer BP. (b) Top view of the crystal structure of monolayer BP and corresponding Brillouin zone. The shadowed rectangle region shows the unit cell with the primitive translational vectors **a** and **b**. (c) The upper panel shows the calculated band structure using the NNTB model, and the lower panel shows the calculated band structure using the VASP (red dashed curves) and WANNIER90 (black solid curves).

and the time-dependent current becomes

$$J(t) = -\sum_{m,n}\int_{BZ}\rho_{nm}^{(W)\boldsymbol{k}_0}(t)\boldsymbol{p}_{mn}^{(W)\boldsymbol{k}(t)}d\boldsymbol{k}. \tag{20}$$

It is worth noting that Eqs. (19) and (20) are essentially the same as the TDSE [22,75].

In our simulation, the electric field $\boldsymbol{E}(t)$ of the laser is given by

$$\boldsymbol{E}_x(t) = \frac{1}{\sqrt{1+\varepsilon^2}}E_0 f(t)\cos(\omega_0 t)\boldsymbol{e}_x,$$
$$\boldsymbol{E}_y(t) = \frac{\varepsilon}{\sqrt{1+\varepsilon^2}}E_0 f(t)\sin(\omega_0 t)\boldsymbol{e}_y, \tag{21}$$

where E_0 is the amplitude of the electric field, ε is the ellipticity, ω_0 is the angular frequency, and $f(t)$ is an eight-cycle trapezoidal envelope whose form is

$$f(t) = \begin{cases} \sin^2(\frac{\pi t}{4T_0}) & -4T_0 \leqslant t < -2T_0, \\ 1 & -2T_0 \leqslant t < 2T_0, \\ \sin^2(\frac{\pi t}{4T_0}) & 2T_0 \leqslant t \leqslant 4T_0, \end{cases} \tag{22}$$

where $T_0 = \frac{2\pi}{\omega_0}$ is an optical cycle. The corresponding vector potential can be obtained by

$$\mathbf{A}(t) = -\int_{-\infty}^{t}\boldsymbol{E}(t')dt'. \tag{23}$$

C. Tight-binding model of monolayer BP

In this subsection, we construct two tight-binding models of monolayer BP. One is obtained from the MLWF method, which uses the WANNIER90 package to process the results from *ab initio* calculations [76,77]. This is referred to as the *ab initio* model in this work. The other one is the NNTB model. Figures 1(a) and 1(b) show the side view and top view of the crystal structure of monolayer BP, respectively.

Obviously, the phosphorus sites are grouped into two zigzag layers [70,78,79].

In the *ab initio* model, the electronic structure information of monolayer BP is obtained by the Vienna *ab initio* simulation package (VASP) [80]. We adopt the exchange-correlation functional of the local density approximation (LDA) and a 20×20 Monkhorst-Pack grid in the calculation. The space group is chosen as *Pmna*. The cutoff energy of the plane-wave basis and the convergence criterion are set as 520 eV and 10^{-8} eV, respectively. Then we perform a projection on the p orbitals and get $\langle \mathbf{0}m|\hat{H}_0|\boldsymbol{R}n\rangle$ and $\langle \mathbf{0}m|\hat{r}|\boldsymbol{R}n\rangle$ using the WANNIER90 package [76,77,81]. The disentanglement energy window is set from -10 eV to 4 eV. Thus the *ab initio* model contains six valence bands and six conduction bands (CBs). In addition, the Hamiltonian obtained by the WANNIER90 may exhibit symmetries that are inconsistent with the crystals due to bad disentanglements. This problem can be resolved by using the numerical tool WANNSYMM to symmetrize the Hamiltonian [82].

In the NNTB model, only the nearest-neighbor interaction is considered, and the Hamiltonian in reciprocal space can be written as [78,79]

$$H_k = \begin{pmatrix} 0 & A_{\boldsymbol{k}} & B_{\boldsymbol{k}} & C_{\boldsymbol{k}} \\ A_{\boldsymbol{k}}^* & 0 & D_{\boldsymbol{k}} & B_{\boldsymbol{k}} \\ B_{\boldsymbol{k}}^* & D_{\boldsymbol{k}}^* & 0 & A_{\boldsymbol{k}} \\ C_{\boldsymbol{k}}^* & B_{\boldsymbol{k}}^* & A_{\boldsymbol{k}}^* & 0 \end{pmatrix}. \tag{24}$$

Here,

$$A_{\boldsymbol{k}} = t_2 + t_5 e^{-ik_a},$$
$$B_{\boldsymbol{k}} = 4t_4 e^{-i(k_a-k_b)/2}\cos(k_a/2)\cos(k_b/2),$$
$$C_{\boldsymbol{k}} = 2e^{ik_b/2}\cos(k_b/2)(t_1 e^{-ik_a} + t_3), \tag{25}$$
$$D_{\boldsymbol{k}} = 2e^{ik_b/2}\cos(k_b/2)(t_1 + t_3 e^{-ik_a}),$$

where $k_a = \boldsymbol{k}\cdot\boldsymbol{a}$ and $k_b = \boldsymbol{k}\cdot\boldsymbol{b}$. $\boldsymbol{a} = a\vec{x}$ and $\boldsymbol{b} = b\vec{y}$ are the primitive translational vectors. The corresponding lattice parameters are set as $a = 4.601$ Å and $b = 3.300$ Å. To compare with our *ab initio* results, the hopping parameters are adjusted as follows: $t_1 = -1.220$ eV, $t_2 = 3.35$ eV, $t_3 = -0.205$ eV, $t_4 = -0.105$ eV, and $t_5 = -0.055$ eV.

The band structure of monolayer BP is displayed in Fig. 1(c). The upper panel shows the result calculated by the NNTB model. This band structure is accurate only within a certain energy range because of the adopted approximations [78]. The lower panel shows the result calculated by the *ab initio* model. For comparison, the band structure calculated by VASP is also given with red dashed curves. It is found that the calculation results of the two methods are very consistent, indicating that our *ab initio* model is valid. In our models, the band gap is 0.89 eV, which is smaller than that in Ref. [69]. This is because we adopt the LDA exchange-correlation functional to compare with the results in Ref. [70]. Previous study has shown that the use of a more advanced exchange-correlation functional can improve the band structure but has no significant effects on the harmonic spectra [70].
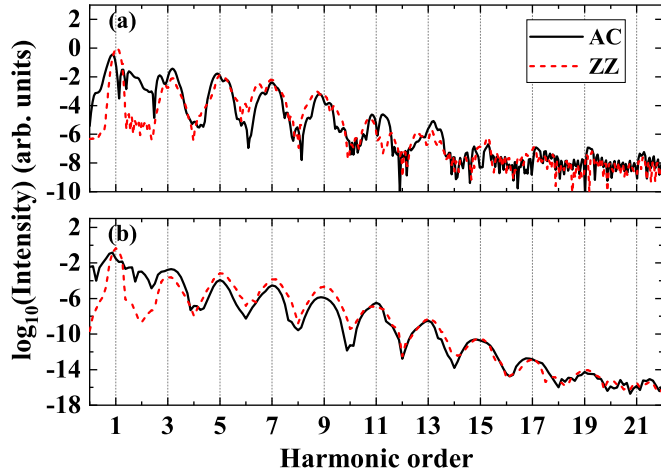
FIG. 2. Harmonic spectra calculated by (a) the TDDFT and (b) the SBEs. The black solid curves and red dashed curves correspond to the laser field polarized along the armchair (AC) and zigzag (ZZ) directions, respectively. The results of TDDFT are reproduced from Ref. [70].

III. RESULTS AND DISCUSSION

A. Limitations of the NNTB approximation

First, we demonstrate the validity of the SBEs represented by the accelerated Bloch-like basis consisting of the MLWF. In this work, we solve the SBEs by the classical fourth-order Runge-Kutta method with the time step of 0.22 a.u. and 200×200 sampling points in the first BZ. The choice of these parameters guarantees the convergence of the results. To compare with the results of the time-dependent density functional theory (TDDFT), we adopt the same laser field in Ref. [70] and set the dephasing time $T_2 = \infty$. Figures 2(a) and 2(b) show the results of the TDDFT in Ref. [70] and our SBEs, respectively. Owing to the inversion symmetry of the system, the harmonic spectra up to the 15th order are composed of only odd harmonics. Notably, our results are in good agreement with those in Ref. [70], demonstrating the validity of our SBEs method.

On this basis, we discuss the limitations of the NNTB approximation. Figure 3(a) presents the harmonic spectra calculated by the NNTB model and the *ab initio* model, respectively. To investigate the limitations of the NNTB approximation, we also neglect the matrix elements of the position operator in the *ab initio* model. We use the linearly polarized laser field in Eq. (21) with $E_0 = 0.002$ a.u. and $\lambda = 3000$ nm, which is polarized along the zigzag direction. The dephasing time is set $T_2 = \infty$ to be consistent with the subsequent results of the TDSE. For comparison, the harmonic spectra calculated by the NNTB model is normalized to the first order of the harmonic spectra calculated by the *ab initio* model. It can be obviously seen that there are significant differences between the two harmonic spectra. For the NNTB model, the intensity of the first few harmonics decreases rapidly, the 11th to 15th harmonics disappear, and the cutoff is around the 19th harmonic. Whereas for the *ab initio* model, a clear plateau can be observed, and the cutoff is around the 23rd harmonic. This indicates the
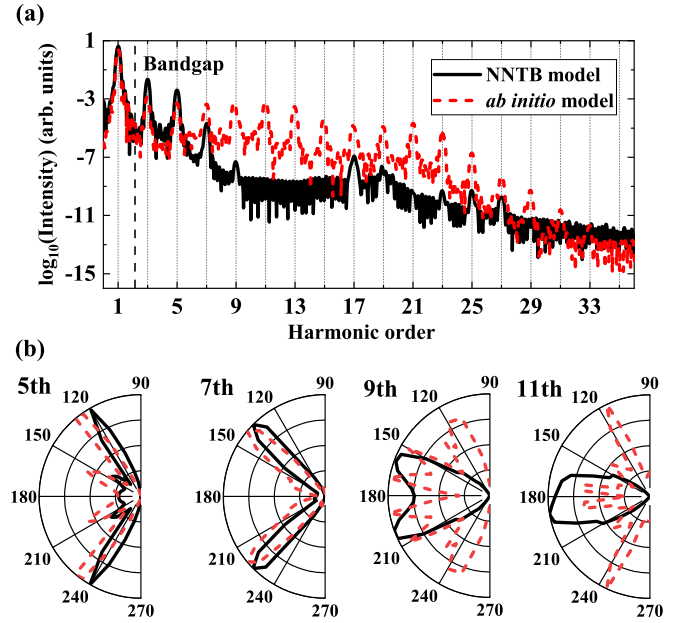

FIG. 3. (a) Harmonic spectra calculated by the SBEs. The vertical dashed line represents the smallest band gap at Γ point. (b) Orientation dependence of harmonic yield. The black solid curves and red dashed curves correspond to the NNTB model and the *ab initio* model, respectively.

limitations of the NNTB approximation in solid HHG calculation, so higher-order interactions need to be considered in tight-binding model. To futher illustrate the limitations of the NNTB approximation, we also investigate the orientation and ellipticity dependence of harmonic yield in monolayer BP.

1. Orientation dependence of harmonic yield

Figure 3(b) shows the orientation dependence of harmonic yield, where the crystal orientation is defined by the relative angle θ between $\mathbf{A}(t)$ and armchair direction as shown in Fig. 1(b). The yield of the nth harmonic is calculated by

$$I_n = \int_{(n-0.5)\omega_0}^{(n+0.5)\omega_0} I(\omega)d\omega. \tag{26}$$

The complex orientation dependence can be observed for monolayer BP. For the fifth harmonic, there are a set of primary maxima around $120°$ and $240°$ and a set of secondary maxima around $150°$ and $210°$. By contrast, the seventh harmonic yield has two maxima around $140°$ and $220°$, and the ninth harmonic yield has six maximum values. This complex orientation dependence is closely related to the electronic structure of monolayer BP as shown in Fig. 1(c) when higher-order interactions are considered. In addition, we also find that the orientation dependence calculated by the two models shows significant differences except for the seventh harmonic. For example, for the fifth harmonic, the orientation dependence calculated by the NNTB model only has two maximum values around $150°$ and $210°$. This implies that the NNTB approximation leads to inaccuracies in calculating the orientation dependence of harmonic yield.

The *ab initio* model includes higher-order interactions and therefore contains more energy bands than the NNTB model.
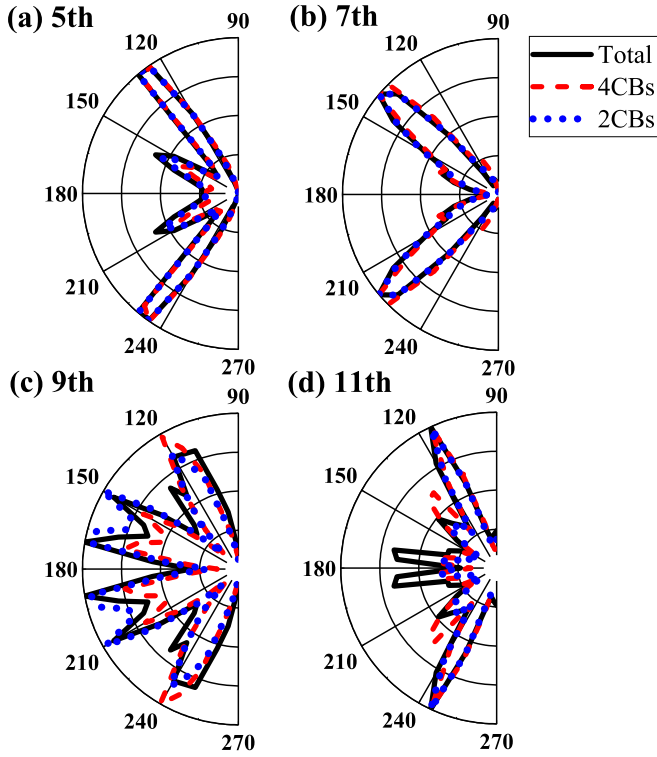
FIG. 4. Orientation dependence of the (a) fifth, (b) seventh, (c) ninth, and (d) 11th harmonic yield. The black solid curves, red dashed curves, and blue dotted curves are the results with six CBs (total), four CBs, and two CBs, respectively.

FIG. 5. Ellipticity dependence of the (a) fifth, (b) seventh, (c) ninth, and (d) 11th harminic yield. The solid curves and dashed curves correspond to the NNTB model and the *ab initio* model, respectively. The red triangle dashed curves and blue square dashed curves are the results without and with the $\hat{r}$ matrix, respectively.

To understand the impact of the multiband effects, we solve the TDSE in the Houston basis. For the specific solution process, please refer to Ref. [83]. According to Eq. (20), we consider the cases of the two lowest, four lowest, and all six CBs, respectively. In the calculation, different bands are distinguished according to the energy. Figure 4 shows the orientation dependence of harmonic yield calculated by the TDSE. By comparing Figs. 3(b) and 4, we find that the results calculated by the TDSE are consistent with those of the *ab initio* model. In addition, for lower-order harmonics such as the fifth and seventh order, the results considering the two and four lowest CBs are consistent with those considering all energy bands. However, as the harmonic order increases, these results gradually show discrepancies. This indicates that the number of CBs needs to be carefully examined when calculating the orientation dependence of harmonic yield.

2. Ellipticity dependence of harmonic yield

Figure 5 shows the ellipticity dependence of harmonic yield, where the elliptical principal axis of the laser field is set along the zigzag direction. As shown, the anomalous ellipticity dependence can be observed for monolayer BP. For the fifth and seventh harmonics, as the ellipticity increases, the yields are almost invariant when $\varepsilon < 0.5$, then increase monotonically when $\varepsilon > 0.5$. Whereas for the ninth harmonic, the yields show a valley around $\varepsilon = 0.3$ and a peak around $\varepsilon = 0.7$. Meanwhile, the 11th harmonic yields are more tortuous and complex. By contrast, for the NNTB model, as the ellipticity increases, all the harmonic yields are invariant when
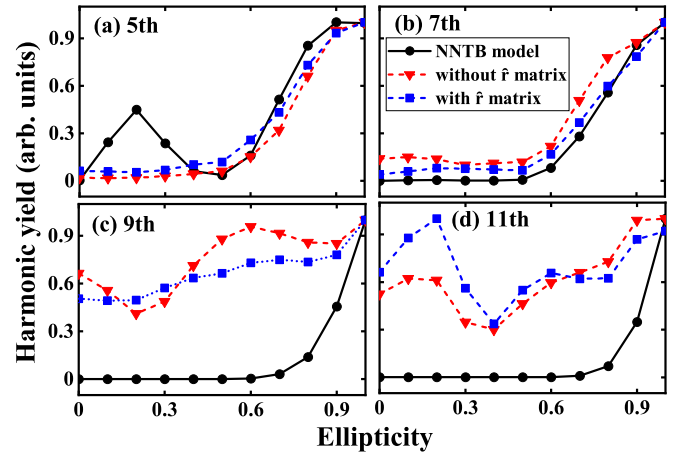
$\varepsilon < 0.5$, then increase monotonically when $\varepsilon > 0.5$, except for the fifth harmonic yield which has a peak at $\varepsilon = 0.2$. These differences provide further evidence for the limitations of the NNTB approximation. Notably, the orientation and ellipticity dependence of the seventh harmonic yield calculated by the two models are well matched. Thus, despite there are some limitations in the NNTB model, it may still be effective in calculating the orientation and ellipticity dependence of certain harmonic yields.

The differences between the two models can be attributed to the differences in the electronic structure information. As shown in Fig. 1(c), the energy band calculated by the NNTB model is accurate only near the Γ point, but is inaccurate in other regions of the first BZ. This will lead to differences in the intraband group velocities and interband transition moments. As a result, there are discrepancies in the dynamics of the electrons and holes in the two models, leading to different harmonic emissions. Finally, these differences are reflected in the orientation and ellipticity dependence of harmonic yield. Therefore, the accuracy of the NNTB approximation should be carefully verified for certain materials.

B. Role of the matrix elements of the position operator

In this subsection, we investigate the role of the matrix elements of the position operator using the *ab initio* model. Figure 6(a) shows the harmonic spectra driven by the laser field polarized along the zigzag direction. It can be seen that the harmonic spectra have no significant variation when the matrix elements of the position operator are neglected. Figure 6(b) further shows the orientation dependence of harmonic yield. We find that the orientation dependence of the fifth and seventh harmonic yields also has no significant variation when neglecting the matrix elements of the position operator. However, for the ninth and 11th harmonic, some discrepancies can be observed. In addition, we also study the impact of the matrix elements of the position operator on the ellipticity dependence of harmonic yield. The results
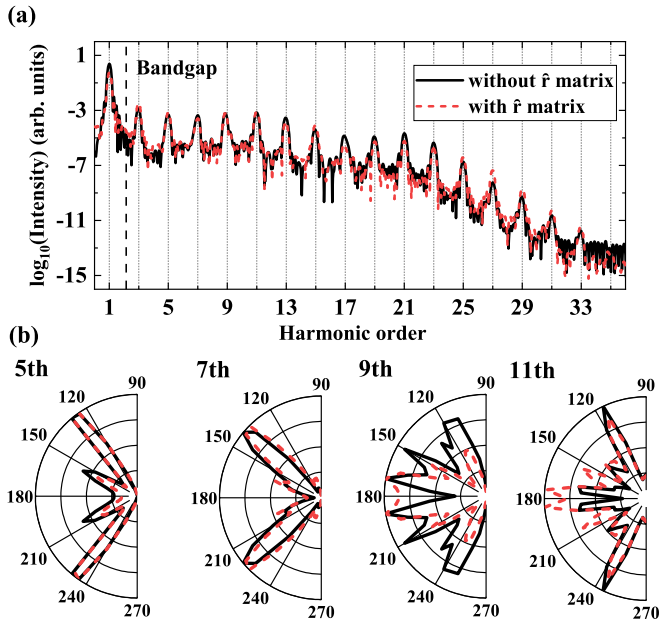
(a)

(b)

FIG. 6. (a) Harmonic spectra calculated by the SBEs. The vertical dashed line represents the smallest band gap at the Γ point. (b) Orientation dependence of harmonic yield. The black solid curves and red dashed curves correspond to the results without and with the $\hat{r}$ matrix, respectively.
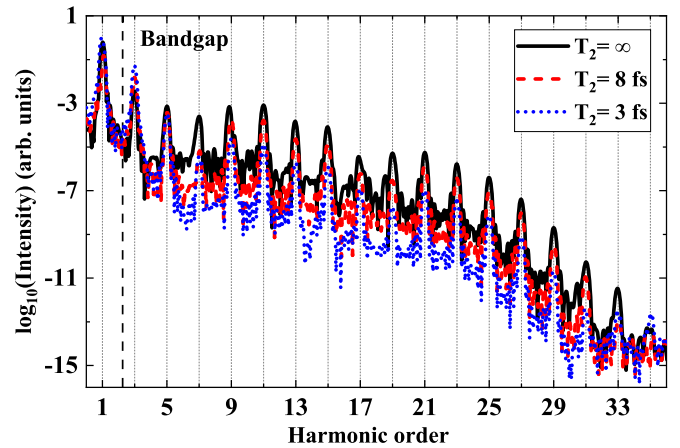

FIG. 7. Harmonic spectra calculated with different dephasing times. The black solid curves, red dashed curves, and blue dotted curves correspond to $T_2 = \infty$, 8 fs, and 3 fs, respectively.

are shown in Fig. 5. When the matrix elements of the position operator are not considered, the ellipticity dependence hardly changes for the fifth and seventh harmonics. However, for higher-order harmonics, such as the ninth and 11th harmonics, although the trend of ellipticity dependence remains unchanged, there are some differences in the harmonic yields. This suggests that the matrix elements of the position operator have an important influence on the orientation and ellipticity dependence of higher-order harmonic yield.

In fact, the diagonal elements of $\langle 0m|\hat{r}|Rn \rangle$ represent the central position of the corresponding atomic orbitals, and the nondiagonal elements represent the hopping of electrons between different atoms and between different atomic orbitals. In the Bloch basis, the matrix of the position operator contains the interband transition elements and the Berry connections [84], which is closely related to the interband recombination process, anomalous Hall current, and topological properties [54,85,86]. It is worth noting that the transition dipole moment in the Wannier basis is different from the transition dipole moment in the Bloch basis. By comparing the interband and intraband currents in Eqs. (16) and Ref. [87], it is obvious that the equations of the intraband current are identical while the equations of the interband current include an additional term that encompasses $A^{(W)}(k)$. We can also transform the SBEs in the Wannier gauge into the Hamilton gauge using the unitary transformations, and the equations will similarly include an additional term of $A^{(W)}(k)$ because of Eq. (5). Our calculations prove that the interband harmonics dominate above the ninth harmonics in monolayer BP (not shown here). Therefore, $A^{(W)}(k)$ only affects the interband current in the calculation, i.e., higher-order harmonics. The correct description of the transition dipole moment is essential for describing the motion of the electrons. Our results indicate that the matrix elements of the position operator can not be neglected arbitrarily.

C. Effect of dephasing times

A proper dephasing time leads to cleaner peaks in the harmonic spectra and thus better match the experimental results as multiple recollisions or long trajectories are suppressed [54,88]. Many elements in the experiment may affect the dephasing time, such as temperature and doping [89], making it difficult to choose a genuine dephasing time in the calculation. In addition, it was found that the dephasing time can be k dependent [90], this property may be more pronounced in anisotropic materials. In our calculation, since the crystal momentum is time-dependent, we need to diagonalize the Hamiltonian matrix $H^{(W)}[k_0 + A(t)]$ to obtain the unitary matrices $U[k_0 + A(t)]$ when transforming Eq. (12) to Eq. (13). This may consume significant computation time and leads to a computational bottleneck in the SBEs with the accelerated Bloch-like basis consisting of the MLWF. For instance, when diagonalization is performed at each time step in the dephasing calculation, the computation time is approximately 2.4 times that without considering the dephasing term. Furthermore, as the size of the Hamiltonian matrix grows, the computation time will further increase. To alleviate the computation burden of diagonalization, the dephasing term can be considered every $N_t(N_t \geqslant 2)$ time steps during the propagation process, provided that the convergence of the results is guaranteed [87]. Figure 7 shows the harmonic spectra calculated with different dephasing times, revealing that shorter dephasing time leads to a lower intensity and cleaner peaks in the harmonic spectra.

IV. CONCLUSION

In summary, the defects of the NNTB model in the study of solid HHG are theoretically investigated. We first develop the SBEs with the accelerated Bloch-like basis consisting of the MLWF and demonstrate the validity by comparing with the calculation results of the TDDFT. Then, we calculate

the harmonic spectra, orientation, and ellipticity dependence of harmonic yield in monolayer BP using the NNTB model and the *ab initio* model, respectively. The complex orientation and anomalous ellipticity dependence of harmonic yield are predicted for monolayer BP. Moreover, we find that the NNTB approximation has limitations in the study of solid HHG. Finally, we explore the role of the matrix elements of the position operator in solid HHG. It is found that these matrix elements have an important effect on the orientation and ellipticity dependence of higher-order harmonic yield and can not be arbitrarily neglected in theoretical calculations. Notably, our conclusions do not mean that the NNTB model is not applicable to all materials, but suggested that the accuracy

of the NNTB model needs to be carefully checked when it is used to study solid HHG.

[1] P. B. Corkum and F. Krausz, Attosecond science, Nat. Phys. **3**, 381 (2007).

[2] F. Krausz and M. Ivanov, Attosecond physics, Rev. Mod. Phys. **81**, 163 (2009).

[3] T. Popmintchev, M.-C. Chen, P. Arpin, M. M. Murnane, and H. C. Kapteyn, The attosecond nonlinear optics of bright coherent X-ray generation, Nat. Photonics **4**, 822 (2010).

[4] F. Silva, S. M. Teichmann, S. L. Cousin, M. Hemmer, and J. Biegert, Spatiotemporal isolation of attosecond soft X-ray pulses in the water window, Nat. Commun. **6**, 6611 (2015).

[5] M. Chini, K. Zhao, and Z. Chang, The generation, characterization and applications of broadband isolated attosecond pulses, Nat. Photonics **8**, 178 (2014).

[6] D. Shafir, H. Soifer, B. D. Bruner, M. Dagan, Y. Mairesse, S. Patchkovskii, M. Y. Ivanov, O. Smirnova, and N. Dudovich, Resolving the time when an electron exits a tunnelling barrier, Nature (London) **485**, 343 (2012).

[7] J. Zhao and M. Lein, Determination of ionization and tunneling times in high-order harmonic generation, Phys. Rev. Lett. **111**, 043901 (2013).

[8] S. Yue, Y. Li, S. Xue, H. Du, and M. Lein, Ionization and recombination times of the long trajectory in high-order harmonic generation, Phys. Rev. A **106**, 023117 (2022).

[9] S. Baker, J. S. Robinson, C. A. Haworth, H. Teng, R. A. Smith, C. C. Chirilă, M. Lein, J. W. G. Tisch, and J. P. Marangos, Probing proton dynamics in molecules on an attosecond time scale, Science **312**, 424 (2006).

[10] M. Lein, Attosecond probing of vibrational dynamics with high-harmonic generation, Phys. Rev. Lett. **94**, 053004 (2005).

[11] L. He, Q. Zhang, P. Lan, W. Cao, X. Zhu, C. Zhai, F. Wang, W. Shi, M. Li, X.-B. Bian *et al.*, Monitoring ultrafast vibrational dynamics of isotopic molecules with frequency modulation of high-order harmonics, Nat. Commun. **9**, 1108 (2018).

[12] J. Itatani, J. Levesque, D. Zeidler, H. Niikura, H. Pépin, J. C. Kieffer, P. B. Corkum, and D. M. Villeneuve, Tomographic imaging of molecular orbitals, Nature (London) **432**, 867 (2004).

[13] S. Ghimire, A. D. DiChiara, E. Sistrunk, P. Agostini, L. F. DiMauro, and D. A. Reis, Observation of high-order harmonic generation in a bulk crystal, Nat. Phys. **7**, 138 (2011).

[14] Y. S. You, D. Reis, and S. Ghimire, Anisotropic high-harmonic generation in bulk crystals, Nat. Phys. **13**, 345 (2017).

[15] N. Tancogne-Dejean, O. D. Mücke, F. X. Kärtner, and A. Rubio, Ellipticity dependence of high-harmonic generation in solids originating from coupled intraband and interband dynamics, Nat. Commun. **8**, 745 (2017).

[16] N. Yoshikawa, T. Tamaya, and K. Tanaka, High-harmonic generation in graphene enhanced by elliptically polarized light excitation, Science **356**, 736 (2017).

[17] X. Zhang, J. Li, Z. Zhou, S. Yue, H. Du, L. Fu, and H.-G. Luo, Ellipticity dependence transition induced by dynamical Bloch oscillations, Phys. Rev. B **99**, 014304 (2019).

[18] C. Liu, Y. Zheng, Z. Zeng, and R. Li, Driving-laser ellipticity dependence of high-order harmonic generation in graphene, Phys. Rev. A **97**, 063412 (2018).

[19] Y. Feng, S. Shi, J. Li, Y. Ren, X. Zhang, J. Chen, and H. Du, Semiclassical analysis of ellipticity dependence of harmonic yield in graphene, Phys. Rev. A **104**, 043525 (2021).

[20] G. Ndabashimiye, S. Ghimire, M. Wu, D. A. Browne, K. J. Schafer, M. B. Gaarde, and D. A. Reis, Solid-state harmonics beyond the atomic limit, Nature (London) **534**, 520 (2016).

[21] Y. S. You, M. Wu, Y. Yin, A. Chew, X. Ren, S. Gholam-Mirzaei, D. A. Browne, M. Chini, Z. Chang, K. J. Schafer *et al.*, Laser waveform control of extreme ultraviolet high harmonics from solids, Opt. Lett. **42**, 1816 (2017).

[22] M. Wu, S. Ghimire, D. A. Reis, K. J. Schafer, and M. B. Gaarde, High-harmonic generation from Bloch electrons in solids, Phys. Rev. A **91**, 043839 (2015).

[23] T.-Y. Du, Z. Guan, X.-X. Zhou, and X.-B. Bian, Enhanced high-order harmonic generation from periodic potentials in inhomogeneous laser fields, Phys. Rev. A **94**, 023419 (2016).

[24] J. B. Li, X. Zhang, S. J. Yue, H. M. Wu, B. T. Hu, and H. C. Du, Enhancement of the second plateau in solid high-order harmonic spectra by the two-color fields, Opt. Express **25**, 18603 (2017).

[25] H. Liu, Y. Li, Y. S. You, S. Ghimire, T. F. Heinz, and D. A. Reis, High-harmonic generation from an atomically thin semiconductor, Nat. Phys. **13**, 262 (2017).

[26] S. Gholam-Mirzaei, J. Beetar, and M. Chini, High harmonic generation in ZnO with a high-power mid-IR OPA, Appl. Phys. Lett. **110**, 061101 (2017).

[27] K. Uchida, V. Pareek, K. Nagai, K. M. Dani, and K. Tanaka, Visualization of two-dimensional transition dipole moment texture in momentum space using high-harmonic generation spectroscopy, Phys. Rev. B **103**, L161406 (2021).

[28] R. Zuo, A. Trautmann, G. Wang, W.-R. Hannes, S. Yang, X. Song, T. Meier, M. Ciappina, H. T. Duc, and W. Yang, Neighboring atom collisions in solid-state high harmonic generation, Ultrafast Science **2021**, 9861923 (2021).

[29] M. S. Mrudul and G. Dixit, High-harmonic generation from monolayer and bilayer graphene, Phys. Rev. B **103**, 094308 (2021).

[30] Y. Ren, L. Jia, Y. Zhang, Z. Zhang, S. Xue, S. Yue, and H. Du, Orientation dependence of even-order harmonics generation in biased bilayer graphene, Phys. Rev. A **106**, 033123 (2022).

[31] T. T. Luu, M. Garg, S. Y. Kruchinin, A. Moulet, M. T. Hassan, and E. Goulielmakis, Extreme ultraviolet high-harmonic spectroscopy of solids, Nature (London) **521**, 498 (2015).

[32] M. Garg, H. Y. Kim, and E. Goulielmakis, Ultimate waveform reproducibility of extreme-ultraviolet pulses by high-harmonic generation in quartz, Nat. Photonics **12**, 291 (2018).

[33] G. Vampa, T. J. Hammond, N. Thiré, B. E. Schmidt, F. Légaré, C. R. McDonald, T. Brabec, D. D. Klug, and P. B. Corkum, All-optical reconstruction of crystal band structure, Phys. Rev. Lett. **115**, 193603 (2015).

[34] L. Li, P. Lan, L. He, W. Cao, Q. Zhang, and P. Lu, Determination of electron band structure using temporal interferometry, Phys. Rev. Lett. **124**, 157403 (2020).

[35] C. Yu, S. Jiang, T. Wu, G. Yuan, Z. Wang, C. Jin, and R. Lu, Two-dimensional imaging of energy bands from crystal orientation dependent higher-order harmonic spectra in $h-$BN, Phys. Rev. B **98**, 085439 (2018).

[36] L. J. Lu and X.-B. Bian, Ultrafast intraband electron dynamics of preexcited SiO$_2$, Opt. Express **28**, 13432 (2020).

[37] A. A. Lanin, E. A. Stepanov, A. B. Fedotov, and A. M. Zheltikov, Mapping the electron band structure by intraband high-harmonic generation in solids, Optica **4**, 516 (2017).

[38] T. T. Luu and H. J. Wörner, Measurement of the Berry curvature of solids using high-harmonic spectroscopy, Nat. Commun. **9**, 916 (2018).

[39] Y. Bai, F. Fei, S. Wang, N. Li, X. Li, F. Song, R. Li, Z. Xu, and P. Liu, High-harmonic generation from topological surface states, Nat. Phys. **17**, 311 (2021).

[40] C. P. Schmid, L. Weigl, P. Grössing, V. Junk, C. Gorini, S. Schlauderer, S. Ito, M. Meierhofer, N. Hofmann, D. Afanasiev *et al.*, Tunable non-integer high-harmonic generation in a topological insulator, Nature (London) **593**, 385 (2021).

[41] R. E. F. Silva, Á. Jiménez-Galán, B. Amorim, O. Smirnova, and M. Ivanov, Topological strong-field physics on sub-laser-cycle timescale, Nat. Photonics **13**, 849 (2019).

[42] C. Heide, Y. Kobayashi, D. R. Baykusheva, D. Jain, J. A. Sobota, M. Hashimoto, P. S. Kirchmann, S. Oh, T. F. Heinz, D. A. Reis *et al.*, Probing topological phase transitions using high-harmonic generation, Nat. Photonics **16**, 620 (2022).

[43] C. Shao, H. Lu, X. Zhang, C. Yu, T. Tohyama, and R. Lu, High-harmonic generation approaching the quantum critical point of strongly correlated systems, Phys. Rev. Lett. **128**, 047401 (2022).

[44] H. Lakhotia, H. Y. Kim, M. Zhan, S. Hu, S. Meng, and E. Goulielmakis, Laser picoscopy of valence electrons in solids, Nature (London) **583**, 55 (2020).

[45] C. Liu, Y. Zheng, Z. Zeng, and R. Li, Effect of elliptical polarization of driving field on high-order-harmonic generation in semiconductor ZnO, Phys. Rev. A **93**, 043806 (2016).

[46] E. N. Osika, A. Chacón, L. Ortmann, N. Suárez, J. A. Pérez-Hernández, B. Szafran, M. F. Ciappina, F. Sols, A. S. Landsman, and M. Lewenstein, Wannier-bloch approach to localization in high-harmonics generation in solids, Phys. Rev. X **7**, 021017 (2017).

[47] S. Jiang, H. Wei, J. Chen, C. Yu, R. Lu, and C. D. Lin, Effect of transition dipole phase on high-order-harmonic generation in solid materials, Phys. Rev. A **96**, 053850 (2017).

[48] S. Jiang, J. Chen, H. Wei, C. Yu, R. Lu, and C. D. Lin, Role of the transition dipole amplitude and phase on the generation of odd and even high-order harmonics in crystals, Phys. Rev. Lett. **120**, 253201 (2018).

[49] J. Li, X. Zhang, S. Fu, Y. Feng, B. Hu, and H. Du, Phase invariance of the semiconductor bloch equations, Phys. Rev. A **100**, 043404 (2019).

[50] N. Marzari and D. Vanderbilt, Maximally localized generalized wannier functions for composite energy bands, Phys. Rev. B **56**, 12847 (1997).

[51] N. Marzari, A. A. Mostofi, J. R. Yates, I. Souza, and D. Vanderbilt, Maximally localized Wannier functions: Theory and applications, Rev. Mod. Phys. **84**, 1419 (2012).

[52] R. E. F. Silva, F. Martín, and M. Ivanov, High harmonic generation in crystals using maximally localized Wannier functions, Phys. Rev. B **100**, 195201 (2019).

[53] J. Li, S. Fu, H. Wang, X. Zhang, B. Ding, B. Hu, and H. Du, Limitations of the single-active-electron approximation in quantum simulations of solid high-order harmonic generation, Phys. Rev. A **98**, 043409 (2018).

[54] G. Vampa, C. R. McDonald, G. Orlando, D. D. Klug, P. B. Corkum, and T. Brabec, Theoretical analysis of high-harmonic generation in solids, Phys. Rev. Lett. **113**, 073901 (2014).

[55] C. Liu, Y. Zheng, Z. Zeng, and R. Li, Polarization-resolved analysis of high-order harmonic generation in monolayer MoS$_2$, New J. Phys. **22**, 073046 (2020).

[56] L. Yue, R. Hollinger, C. B. Uzundal, B. Nebgen, Z. Gan, E. Najafidehaghani, A. George, C. Spielmann, D. Kartashov, A. Turchanin *et al.*, Signatures of multiband effects in high-harmonic generation in monolayer MoS$_2$, Phys. Rev. Lett. **129**, 147401 (2022).

[57] C. Vaswani, M. Mootz, C. Sundahl, D. H. Mudiyanselage, J. H. Kang, X. Yang, D. Cheng, C. Huang, R. H. J. Kim, Z. Liu *et al.*, Terahertz second-harmonic generation from lightwave acceleration of symmetry-breaking nonlinear supercurrents, Phys. Rev. Lett. **124**, 207003 (2020).

[58] D. Kim, Y. Lee, A. Chacón, and D.-E. Kim, Effect of interlayer coupling and symmetry on high-order harmonic generation from monolayer and bilayer hexagonal boron nitride, Symmetry **14**, 84 (2022).

[59] X.-Y. Wu, H. Liang, X.-S. Kong, Q. Gong, and L.-Y. Peng, Multiscale numerical tool for studying nonlinear dynamics in solids induced by strong laser pulses, Phys. Rev. E **105**, 055306 (2022).

[60] J. Ibañez-Azpiroz, F. de Juan, and I. Souza, Assessing the role of interatomic position matrix elements in tight-binding calculations of optical properties, SciPost Phys. **12**, 070 (2022).

[61] K. S. Novoselov, A. K. Geim, S. V. Morozov, D. Jiang, Y. Zhang, S. V. Dubonos, I. V. Grigorieva, and A. A. Firsov, Electric field effect in atomically thin carbon films, Science **306**, 666 (2004).

[62] A. K. Geim and K. S. Novoselov, The rise of graphene, Nat. Mater. **6**, 183 (2007).

[63] B. Radisavljevic, A. Radenovic, J. Brivio, V. Giacometti, and A. Kis, Single-layer MoS$_2$ transistors, Nat. Nanotechnol. **6**, 147 (2011).

[64] Q. H. Wang, K. Kalantar-Zadeh, A. Kis, J. N. Coleman, and M. S. Strano, Electronics and optoelectronics of two-dimensional transition metal dichalcogenides, Nat. Nanotechnol. **7**, 699 (2012).

[65] J. D. Cox, A. Marini, and F. J. G. de Abajo, Plasmon-assisted high-harmonic generation in graphene, Nat. Commun. **8**, 14380 (2017).

[66] N. Tancogne-Dejean and A. Rubio, Atomic-like high-harmonic generation from two-dimensional materials, Sci. Adv. **4**, eaao5207 (2018).

[67] L. Li, Y. Yu, G. J. Ye, Q. Ge, X. Ou, H. Wu, D. Feng, X. H. Chen, and Y. Zhang, Black phosphorus field-effect transistors, Nat. Nanotechnol. **9**, 372 (2014).

[68] F. Xia, H. Wang, and Y. Jia, Rediscovering black phosphorus as an anisotropic layered material for optoelectronics and electronics, Nat. Commun. **5**, 4458 (2014).

[69] J. Qiao, X. Kong, Z.-X. Hu, F. Yang, and W. Ji, High-mobility transport anisotropy and linear dichroism in few-layer black phosphorus, Nat. Commun. **5**, 4475 (2014).

[70] Z. Y. Chen and R. Qin, Strong-field nonlinear optical properties of monolayer black phosphorus, Nanoscale **11**, 16377 (2019).

[71] X. Wang, J. R. Yates, I. Souza, and D. Vanderbilt, *Ab initio* calculation of the anomalous Hall conductivity by Wannier interpolation, Phys. Rev. B **74**, 195118 (2006).

[72] W. V. Houston, Acceleration of electrons in a crystal lattice, Phys. Rev. **57**, 184 (1940).

[73] J. B. Krieger and G. J. Iafrate, Time evolution of Bloch electrons in a homogeneous electric field, Phys. Rev. B **33**, 5494 (1986).

[74] J. B. Krieger and G. J. Iafrate, Quantum transport for Bloch electrons in a spatially homogeneous electric field, Phys. Rev. B **35**, 9644 (1987).

[75] Z. Guan, X.-X. Zhou, and X.-B. Bian, High-order-harmonic generation from periodic potentials driven by few-cycle laser pulses, Phys. Rev. A **93**, 033852 (2016).

[76] A. A. Mostofi, J. R. Yates, Y.-S. Lee, I. Souza, D. Vanderbilt, and N. Marzari, wannier90: A tool for obtaining maximally-localised Wannier functions, Comput. Phys. Commun. **178**, 685 (2008).

[77] G. Pizzi, V. Vitale, R. Arita, S. Blügel, F. Freimuth, G. Géranton, M. Gibertini, D. Gresch, C. Johnson, T. Koretsune *et al.*, WANNIER90 as a community code: New features and applications, J. Phys.: Condens. Matter **32**, 165902 (2020).

[78] A. N. Rudenko and M. I. Katsnelson, Quasiparticle band structure and tight-binding model for single- and bilayer black phosphorus, Phys. Rev. B **89**, 201408(R) (2014).

[79] E. Taghizadeh Sisakht, M. H. Zare, and F. Fazileh, Scaling laws of band gaps of phosphorene nanoribbons: A tight-binding calculation, Phys. Rev. B **91**, 085409 (2015).

[80] G. Kresse and J. Furthmüller, Efficient iterative schemes for *ab initio* total-energy calculations using a plane-wave basis set, Phys. Rev. B **54**, 11169 (1996).

[81] C. Xiao, The VASP2WAN90_v2_fix patch, https://github.com/Chengcheng-Xiao/VASP2WAN90_v2_fix/.

[82] G.-X. Zhi, C. Xu, S.-Q. Wu, F. Ning, and C. Cao, WannSymm: A symmetry analysis code for Wannier orbitals, Comput. Phys. Commun. **271**, 108196 (2022).

[83] P. G. Hawkins, M. Y. Ivanov, and V. S. Yakovlev, Effect of multiple conduction bands on high-harmonic emission from dielectrics, Phys. Rev. A **91**, 013405 (2015).

[84] L. Yue and M. B. Gaarde, Introduction to theory of high-harmonic generation in solids: tutorial, J. Opt. Soc. Am. B **39**, 535 (2022).

[85] M. Gradhand, D. V. Fedorov, F. Pientka, P. Zahn, I. Mertig, and B. L. Györffy, First-principle calculations of the berry curvature of bloch states for charge and spin transport of electrons, J. Phys.: Condens. Matter **24**, 213202 (2012).

[86] M. Wimmer, H. M. Price, I. Carusotto, and U. Peschel, Experimental measurement of the Berry curvature from anomalous transport, Nat. Phys. **13**, 545 (2017).

[87] L. Yue and M. B. Gaarde, Structure gauges and laser gauges for the semiconductor Bloch equations in high-order harmonic generation in solids, Phys. Rev. A **101**, 053411 (2020).

[88] Y. W. Kim, T.-J. Shao, H. Kim, S. Han, S. Kim, M. Ciappina, X.-B. Bian, and S.-W. Kim, Spectral interference in high harmonic generation from solids, ACS Photonics **6**, 851 (2019).

[89] T.-Y. Du and C. Ma, Temperature-induced dephasing in high-order harmonic generation from solids, Phys. Rev. A **105**, 053125 (2022).

[90] G. Wang and T.-Y. Du, Quantum decoherence in high-order harmonic generation from solids, Phys. Rev. A **103**, 063109 (2021).